Geosci. Model Dev. Discuss., 6, 3381–3426, 2013
www.geosci-model-dev-discuss.net/6/3381/2013/
doi:10.5194/gmdd-6-3381-2013

Geoscientific Model Development Discussions
Open Access

TopoSCALE: deriving surface fluxes from gridded climate data

J. Fiddes and S. Gruber

Glaciology, Geomorphodynamics & Geochronology, Department of Geography, University of Zurich, Zurich, Switzerland

Received: 26 April 2013 – Accepted: 29 May 2013 – Published: 26 June 2013

Correspondence to: J. Fiddes (joel.fiddes@geo.uzh.ch)

Published by Copernicus Publications on behalf of the European Geosciences Union.

Abstract

Simulation of land surface processes is problematic in heterogeneous terrain due to the the high resolution required of model grids to capture strong lateral variability caused by e.g. topography and the lack of accurate meteorological forcing data at the site or scale it is required. Gridded data products produced by atmospheric models can fill this gap, however, often not at an appropriate spatial resolution to drive land-surface simulations. In this study we describe a method that leverages the good description of the atmospheric column provided by climate models, together with high resolution DEM's, to derive a consistent topography-based, scaling of coarse grid climate variables to fine-scale. We test the method together with unscaled grid-level data and a set of reference methods, against a large evaluation dataset (up to 210 stations per variable) in the Swiss Alps. We demonstrate that the method can be used to derive meteorological inputs in complex terrain, with most significant improvements (with respect to reference methods) seen in variables derived from pressure-levels: air temperature, relative humidity, wind speed and incoming longwave radiation. It is expected that this method can be used to improve inputs to numerical simulations in complex and/or remote terrain especially when statistical methods are not possible due to lack of observations i.e. remote areas or future periods.

1 Introduction

Simulations of land surface processes are important for performing assessments of a wide-range of earth-systems, under current and possible future climates. This task is problematic in complex terrain due to the inter-connected problems of: (i) the high resolution required of model grids to capture strong lateral variability caused by e.g. topography, surface or sub-surface processes (e.g. Gubler et al., 2011; Riseborough et al., 2008; Arnold and Rees, 2009), and consequently, (ii) the lack of accurate meteorological forcing data at the site or scale it is required (Thornton et al., 1997; Liston and Elder, 2006). This can be due to the lack of meteorological observations (i.e. spatial

GMDD
6, 3381–3426, 2013

coverage, temporal extent/continuity, or variables measured are insufficient for purpose) or lack of representative observations where surface variability is high. Gridded data products produced by atmospheric models can, in part, fill this gap (e.g. Frauenfeld, 2005; Pereira-Cardenal et al., 2011; Akhtar et al., 2009; Vu et al., 2012). However, in many cases not at an appropriate spatial resolution to drive land-surface simulations (i.e. site scale), and therefore require some form of downscaling of variables.

Downscaling of climate data can be broadly divided into dynamical or statistical methods (Schmidli et al., 2007) which are used to increase the resolution of large scale climate fields by approximately an order of magnitude i.e. 10^2–10^1 km, see for full discussion Wilby and Wigley (1997). Dynamical methods achieve this by using a limited area model at a higher grid resolution e.g. a regional climate model (RCM), to simulate fine-scale proccesses which are consistent with large-scale climate fields (Giorgi, 2006). While an RCM grid resolution could be increased further, in practice the effective resolution is currently limited by the complexity of the numerics that must be solved at each time-step, to the order of 10^1 km (Kotlarski and Block, 2005). Statistical methods derive empirical relationships between large scale predictor fields and local observations (Maraun and Wetterhall, 2010). These methods are computationally efficient but the coverage and effective resolution is often limited by the density of observations, especially in mountainous (i.e. data-poor) areas. Additionally, it is unknown whether empirically derived relationships are valid outside the time window used for calibration. To compliment these approaches there is a growing number of physically-inspired, computationally efficient approaches that use physical relationships and high resolution surface information (i.e. DEMs) to distribute fine-scale forcings (meteorological stations or coarse-grid centre point) over wide areas (e.g. Liston and Elder, 2006; Tarboton and Luce, 1996; Marks et al., 1999; Jarosch et al., 2012). These distributed forcings can then be used for full 2-D, point scale or lumped model simulations.

In complex terrain, topography-based gradients (i.e. related to elevation, aspect, slope etc.) of meteorological variables can often dominate over the horizontal (i.e. latitude/longitude) within a region that is of comparable size to a typical coarse climate cell

GMDD
6, 3381–3426, 2013

(e.g. 50–100 km). An example of a method that has successfully encoded this assumption is the PRISM framework (parameter-elevation regressions on independent slopes model) which provides a statistical, topography-based mapping of climate observations (Daly et al., 1994, 2002). Climate models provide spatially and temporally continuous fields which are physically consistent and therefore are useful tools for forcing regional scale land-surface studies (Machguth et al., 2009; Kotlarski et al., 2010). In addition, they provide a thorough description of the atmospheric column by providing data fields at many pressure levels between the Earth's surface and top of the atmosphere.

The aim of this study is to develop methods that leverage the good description of the atmospheric column and surface fields provided by climate models, together with high resolution DEM's, to derive a consistent (methodologically, spatially, temporally) and physically realistic, scaling of coarse grid climate variables to a sub-grid domain. These downscaled fields can then be used to drive a land surface model (LSM). With this in mind, the design criteria for the present method are: (1) it provides a high resolution (< 100 m) scaling of climate data based primarily on topographic information; (2) it is as physically based as possible; (3) it has minimal reliance on observations; (4) it likely remains valid under future conditions; (5) it employs simple methods which are computationally efficient; (6) it may be used as part of a modelling chain with a lumped representation of the subgrid domain (e.g. Fiddes and Gruber, 2012) for large area applications, as well as 1-D points and 2-D grids. Our approach therefore largely assumes vertical gradients to dominate horizontal gradients within a given model grid box. In this study, we describe this method and its application with ERA-Interim data, a 4-D-VAR reanalysis (3rd generation) which uses the ECMWF climate model, although the method could be equally used with other reanalyses, e.g. NARR, NCEP/NCAR, JRA-55 or NASA MERRA, RCM or GCM derived fields. Our methods are then evaluated against a large number of observations over a wide area of complex terrain in the European Alps as well as compared to a set of reference methods. The methods proposed here aim to provide an alternative to statistical methods when observations

GMDD
6, 3381–3426, 2013

are not available (remote areas or future periods) and be complimentry to dynamical methods i.e. they could be used to further downscale RCM output to site scale.

2 Background

Reanalyses are complex products in that they combine a climate model with observations. This section provides background information on reanalysis in general and ERA-Interim specifically, in order to place this study and results in context, as well as to highlight some important limitations to this approach.

2.1 Assimilation issues

Reanlyses assimilate large numbers of observations in spatially and temporally varying quantities/densities. It is important to understand what data is assimilated into the ERA-I product as this not only affects how independent observations are in terms of validation but also gives some idea of how the performance of ERA-I can vary with regional observation density. Assimilated data that is also used for evaluation in this study comes from the SYNOP registered MeteoSchweiz stations (a subset of the ANETZ network), and only affects observations of air temperature and relative humidity (Table 1). Furthermore, for screen-level analysis (2 m temperature, 2 m relative humidity) surface observations that differ by more that 300 m from the model orography are rejected in the ERA-I assimilation. Further details are given in Sect. 4.2. In general, assimilated observations are not scaled (P. Berrisford, personal communication, 2013), see ECMWF (2011) for further details.

2.2 Bias and spatial/temporal variability of errors

LSM results are sensitive to bias in climate data (e.g. Berg, 2003), and bias correction is usually regarded as a crucial step in providing accurate driving fields to a land-surface or impact model (Hagemann et al., 2011). In this study we choose to conceptually

GMDD
6, 3381–3426, 2013

separate “bias” and “scale” (often combined in downscaling routines based on station data) in order to focus on the problem of topography-based scaling, as this is not reliant on observational datasets. Therefore, the treatment of bias can be performed in a second step with a reduced influence of scale. However, we acknowledge that bias correction is often necessary to provide accurate fields to impact models. Reanalysis can be seen as an imperfect model combined with incomplete data and their output should not be equated with “observations” or “reality”. The changing mix of observations, and biases in observations and models, can introduce spurious variability and trends into reanalysis output. Observational constraints, and therefore reanalysis reliability, can vary considerably depending on the location, time period, and variable considered. Another problem is that mixing observations with models tends to violate conservation laws. Most significant to this study is the fact that re-analysis will likely be closer to reality at locations with higher observation densities i.e Europe and specifically the European Alps in contrast to other high mountain regions.

2.3 Sub-grid issues and boundary-layer effects

Due to the coarse resolution of current re-analysis datasets (typically 0.75–1.5 °), various processes are unresolved by the model. An important example is temperature inversion in mountain valleys, which will not be captured by the data. Another important process is local-scale rain shadows caused by unresolved topographic barriers and, additionally, shallow convection in warmer months. The surface boundary layer (as opposed atmospheric boundary layer) will have a residual effect upon surface measurements, which will not necessarily be present in pressure-levels representing the free atmosphere. For example, turbulent exchanges of sensible heat fluxes can be a significant contributer to energy exchange between surface and atmosphere (Cline, 1997; Helgason and Pomeroy, 2012). These effects will also likely affect diurnal cycles of observations. However, the magnitude of these effects is not quantified by this study.

GMDD
6, 3381–3426, 2013

2.4 Pressure levels below model surface

While model levels are computed from the terrain surface to top of the atmosphere, pressure level data is given in the interval 1000 mb (approximately sea level)–1 mb (top of atmosphere). This means that pressure level data exists below the model-grid surface in regions with rugged topography. The extrapolation of fields below the surface uses different methods to those above surface, additionally a greater quantity of data is assimilated from above surface observations. Therefore, it can be expected that there is a difference in quality of above/below grid pressure level data. In addition, measurement locations below grid level are more likely to be in valleys and therefore greater exposure of observations to sub-grid phenomenon, not represented by the data. See ECMWF (2011) for full details of extrapolation methods. However, it is difficult to disentangle this effect from the fact that measurements above the model surface are more likely to represent the free atmosphere and, therefore, be more accurately simulated than those strongly effected by topographic effects (e.g. Mesinger et al., 2006; Jarosch et al., 2012) such as inversion layers or topographically modified wind fields. This issue is addressed in the results section.

3 Methods

3.1 TopoSCALE

We downscale the variables required to drive an LSM from ERA-I pressure-level (PL) and grid-surface (GRID) fields (Table 1). Input pressure-level fields used are, air temperature (T_{pl}), relative humidity (Rh_{pl}), wind components U and V, which are converted to wind speed (Ws_{pl}). Input grid-surface fields are downwelling global radiation ($SW{\downarrow}_{grid}$), downwelling longwave radiation ($LW{\downarrow}_{grid}$) and precipitation (P_{grid}). Accumulated values of $SW{\downarrow}_{grid}$ and $LW{\downarrow}_{grid}$ are converted to timestep averages of $W\,m^{-2}$ and accumulated P_{grid} is converted to a mean rate of $mm\,h^{-1}$, prior to scaling. The temporal

GMDD
6, 3381–3426, 2013

resolution of surface fields is 3 h and PL fields, with native resolution of 6 h, are interpolated to the same 3 h timestep. Additionally, the fields T_{grid}, Rh_{grid} and SW_{toa} are used indirectly for radiation computations. Locations at the coarse grid level or the fine-scale subgrid are referred to as GRID and SUB, respectively.

3.1.1 Pressure-level fields

Fields derived from pressure-levels, T_{sub}, Rh_{sub}, Ws_{sub} are computed directly from pressure level data in two steps: (1) pressure-level elevations (m a.s.l.) are estimated in a standard way by normalising geopotential heights by gravity at sea level (Appendix A). (2) Value at SUB elevation is linearly interpolated from data at pressure-levels above and below SUB elevation (Fig. 2). Ws_{sub} is derived from U and V wind components after interpolation. Topographically modified wind fields are then computed according to a simple wind model (Liston and Sturm, 1998) which adjusts the speeds and directions according to topographic slope and curvature relationships. To perform the wind modification calculations, the local slope, aspect, and topographic curvature (a measure of relative prominance with respect to surrounding terrain) are required (Appendix B).

3.1.2 Radiative fluxes

$LW{\downarrow}_{sub}$ is computed by deriving a cloud-component of all-sky emmissivity at grid level and using T_{sub}, Rh_{sub} to describe variability with elevation. First, clear-sky emissivity at SUB (ϵ^{cl}_{sub}) and GRID (ϵ^{cl}_{grid}) are computed according to Konzelmann et al. (1994),

$$\epsilon^{cl} = 0.23 + x1(pV/T)^{1/x2} \quad (1)$$

where $x1 = 0.43$ and $x2 = 5.7$ (Gubler et al., 2012) and water vapour pressure, pV is a function of Rh (Appendix A). The all-sky emissivity is computed at GRID using $LW{\downarrow}_{grid}$ and the Stefan–Boltzmann equation,

$$\epsilon^{as}_{grid} = LW{\downarrow}_{grid} / \sigma T^4_{grid} \quad (2)$$

GMDD
6, 3381–3426, 2013

where σ is the Stefan Boltzmann constant of $5.67 \times 10^{-8} \mathrm{Js}^{-1}\mathrm{m}{-}2\mathrm{K}^{-4}$. We estimate the cloud-based component of emissivity ($\Delta\epsilon$) at GRID though subtraction of $\epsilon^{\mathrm{cl}}_{\mathrm{grid}}$ from $\epsilon^{\mathrm{as}}_{\mathrm{grid}}$ in order to apply this correction directly at SUB. Finally $\mathrm{LW}\downarrow_{\mathrm{sub}}$ can be computed accounting for elevation changes in T and Rh by,

$$\mathrm{LW}\downarrow_{\mathrm{grid}} = \left(\epsilon^{\mathrm{cl}}_{\mathrm{sub}} + \Delta\epsilon\right)\sigma T^4_{\mathrm{sub}} \quad (3)$$

This approach assumes that cloud emmissivity at GRID and SUB elevations are the same, but accounts for reduction of clear-sky emissivity with elevation. This is important as the steepest gradients in LW↓ are often found in clear-sky conditions due to reduction in atmospheric water vapour with elevation. After elevation correction, terrain effects are accounted for by reduction of $\mathrm{LW}\downarrow_{\mathrm{sub}}$ by multiplication with the sky-view factor, being the fraction of sky that is visible at SUB (V_{d}). This assumes that LW↓ is isotropic.

$\mathrm{SW}\downarrow_{\mathrm{sub}}$ is computed in a three step process: (1) partitioning of $\mathrm{SW}\downarrow_{\mathrm{grid}}$ into direct and diffuse components, (2) elevation adjustment of direct, and (3) topographic correction of both diffuse and direct at point scale. $\mathrm{SW}\downarrow_{\mathrm{grid}}$ can be partitioned into direct ($\mathrm{SW}\downarrow^{\mathrm{dir}}_{\mathrm{grid}}$) and and diffuse ($\mathrm{SW}\downarrow^{\mathrm{dif}}_{\mathrm{grid}}$) components according to the hourly regression model of Ruiz-Arias et al. (2010b) which has been developed based on 21 stations in Europe and USA (Appendix A). This method uses the clearness index, which is computed by ratioing $\mathrm{SW}\downarrow_{\mathrm{grid}}$ against irradiance at top of atmosphere, $\mathrm{SW}\downarrow_{\mathrm{toa}}$ (Appendix A) and in doing so estimates a solar transmissivity of the atmospheric column (Fig. 3a). It should be noted that the regression model was developed on hourly data, whereas we apply it to 3 h averages. The vertical gradient of global irradiance between GRID and SUB is mainly determined by the direct component together with difference in the optical path length Δm, assuming that attenuative properties of the atmosphere are constant between the two elevations. Therefore, we apply an elevation correction to $\mathrm{SW}\downarrow^{\mathrm{dir}}_{\mathrm{grid}}$ only, largely following methods of Ruiz-Arias et al. (2010b) (Fig. 3b). First, Δm is computed as,

$$\Delta m = \Delta z \cos\theta_z, \quad (4)$$

GMDD
6, 3381–3426, 2013

where Δz is difference in elevation and θ_z is the solar zenith angle. We can then solve the Beer–Lambert law for direct irradiance to obtain the broadband attenuation coefficient, k,

$$\mathrm{SW}\downarrow^{\mathrm{dir}} = \mathrm{SW}\downarrow^{\mathrm{toa}} e^{-km} \tag{5}$$

where $m = 1/\cos\theta_z$ (except for large values of θ_z). The difference in $\mathrm{SW}\downarrow^{\mathrm{dir}}$ (δ) due to elevation difference between GRID and SUB can then be found as:

$$\frac{\Delta \mathrm{SW}\downarrow^{\mathrm{dir}}}{\mathrm{SW}\downarrow^{\mathrm{dir}}} \approx 1 - e^{-k\Delta z \cos\theta_z} \tag{6}$$

Equation (6) shows direct irradiance should increase exponentially with elevation given constant k and elevation based change in irradiance is maximum when sun is at zenith and zero when sun is at horizon. As the correction is only aplicable to clear-sky conditions, it is applied when the airmass-corrected clearness index K_t is greater than 0.65 (Perez et al., 1990).

$\mathrm{SW}\downarrow^{\mathrm{dir}}_{\mathrm{sub}}$ is computed by correcting for terrain effects of slope, aspect and horizon at SUB according to Dozier and Frew (1990) and Dubayah and Rich (1995) (Fig. 3c). This is achieved by computing the illumination angle i, which is the angle the incident direct beam makes with the slope normal and varies with solar zenith θ_0 and azimuth angles ϕ_0 and local slope angle S and aspect A:

$$\cos i_{\mathrm{sub}} = \cos\theta_z \cos S + \sin\theta_z \sin S \cos(\phi_0 - A) \tag{7}$$

By ignoring variation in latitude and longitude within a given grid box θ_z and ϕ_0 can remain constant, which over short length scales is a reasonable simplication (e.g. Dozier and Frew, 1990). As slope = 0 at GRID, $\cos i_{\mathrm{grid}}$ is simply given by

$$\cos i_{\mathrm{grid}} = \cos\theta_z. \tag{8}$$

Additionally, cast-shadows and self-shadowing effects are often important in complex terrain and are accounted for through local horizon elevations. Wherever $\cos i_{\mathrm{sub}}$ is

GMDD
6, 3381–3426, 2013

negative, the point is self-shadowed i.e. the sun is below the horizon formed by the local slope and $SW\downarrow_{sub}^{dir}$ is set to 0. Cast shadows are found by horizon elevations and given as δ, a binary shadow mask. Topographically corrected $SW\downarrow_{sub}^{dir}$ is then given by first removing the GRID cosine correction and then multiplying by SUB cosine correction:

$$SW\downarrow_{sub}^{dir} = SW\downarrow_{dir} \frac{\cos i_{sub}}{\cos i_{grid}} \delta \quad (9)$$

where horizon elevations are either explicitly given in n directions for 1-D/2-D simulations or parameterised for use with a lumped scheme (e.g. Fiddes and Gruber, 2012) as a function of local slope and V_d in order to detect shading. Computation of $SW\downarrow_{sub}^{dif}$ assuming isotropy requires only V_d:

$$SW\downarrow_{sub}^{dif} = SW\downarrow_{grid}^{dif} V_d. \quad (10)$$

3.1.3 Precipitation

Precipitation in mountain regions occurs due to a range of complex mechanisms which depend upon e.g. season, geographical climate (maritime, continental) and structure of orography. Precipitation is therefore strongly variable in both time and space. We apply a combined climatology and lapse rate approach (e.g. Früh et al., 2006). We acknowledge that the quality of the datset is heavily dependent on density of observations and therefore, better than average results should be expected in our study domain. First, the dependence on elevation is removed by inverting the non-linear lapse rate of Liston and Elder (2006) (Appendix A), then normalising to the GRID reference elevation. P_{grid} is then dissagregated according to the sub-grid variability (now elevation independent) as described by the climatology. That is, each of the i-th (in this study 1–25) climatology grid-cells P_{clim} are normalised by the sum of grid-cells contained in each ERA course grid box, resulting in a sub-grid disagregation factor W_{sub}:

$$W_{sub} = P_{clim}^{i} / \sum P_{clim}. \quad (11)$$

GMDD
6, 3381–3426, 2013

In this study we use the CRU climatology (cf. Sect. 4) but other sources of sub-grid observations could be used. Globally, or near globally available datasets (gauge and satellite based) include the Tropical Rainfall Measuring Mission (Huffman et al., 2007), Global Preciptiation Climatology Centre (Beck et al., 2005) and Climatic Research Unit (New et al., 2002) or regionally available such as PRISM (Daly et al., 1994) or even direct observations if available. The product of P_{grid} and W_{sub} generates a sub-grid distribution of precipitation at CRU resolution that is conservative of the coarse grid forcing P_{grid}. Finally, the same non-linear lapse rate used to remove elevation dependence is applied to capture fine scale precipitation-elevation gradients to scale from GRID to SUB (Liston and Elder, 2006).

3.2 Reference methods

The following is a description of the reference parameterisations with which we compare the current scheme. We do not intend this comparison to be exhaustive, but to merely serve as a reference point.

T_{grid} is simply extrapolated according to a fixed lapse of 6.5 °C km^{-1} (e.g. Blandford et al., 2008). Rh is not a linear function of elevation and so the relatively linear dewpoint temperature (Td) is often used (Liston and Elder, 2006). Rh can be converted to Td as a function of T and saturation vapour pressure (Appendix A). In this study Td_{grid} is available, so this step is unnecessary.

Td_{sub} can be computed using a variable lapse rate (Kunkel, 1989):

$$\text{lapse} = \lambda \cdot c/b \tag{12}$$

where λ is a vapour pressure coefficient that varies during each month of the year (Kunkel, 1989). Finally, Td_{sub} is then converted back to Rh_{sub} as a function of T_{sub}. LW↓ is parameterised as a function of T and pV and cloud cover according to the clear-sky formula of Konzelmann et al. (1994) (Eq. 1) and the all-sky formula of Pirazzini et al.

GMDD
6, 3381–3426, 2013

(2000) while accounting for V_d,

$$\mathrm{LW}\downarrow = \epsilon^{\mathrm{cl}}(1 - N^{p1}) + \left(\epsilon^{\mathrm{as}} N^{p2}\right)\sigma T^4, \quad (13)$$

where ϵ^{cl} is given by Eq. (1), N is given by the ERA-I total cloud product (0–1), $p1 = 6$, $p2 = 4$ and $\epsilon^{\mathrm{as}} = 0.979$. Wind is adjusted by 40 % per km i.e increased above grid level reduced below grid level (Plüss, 1997). SW↓ is not compared to a reference method as the methods (i.e. partitioning, elevation and topograhic correction) used in this study are commonly used elsewhere (i.e. Oliphant, 2003; Schroeder et al., 2009). Precipitation is scaled with a non-linear lapse rate (Liston and Elder, 2006).

3.3 Temporal interpolation and time-zones

The primary purpose of this scheme is to deliver input variables to a numerical LSM. Therefore, sub-daily variables are needed. We include in the scheme a simple linear interpolation to increase resolution of pressure-level data (6 h) to surface fields (3 h). An additional step is necessary for accummulated fields (radiation and precipitation) as they represent totals since start of forecast at each time-step. To obtain the average between two forecast steps (e.g. stp1 and stp2), the fields for the two steps are retrieved (e.g. $\mathrm{field}_{\mathrm{stp1}}$ and $\mathrm{field}_{\mathrm{stp2}}$) then the difference is calculated and divided by the time difference in seconds (Δt),

$$\mathrm{field}_{\mathrm{average}} = \mathrm{field}_{\mathrm{stp2}} - \mathrm{field}_{\mathrm{stp1}}/\Delta t. \quad (14)$$

This will then give average values at timestep midpoints i.e. 01:30–22:30 UTC in 3 h steps. To obtain values at timepoints consistent with other variables an average over the time since the previous time-step is taken. Finally, a timezone correction is applied to native UTC timezone of ERA-I. The final output has all variables given at a consistent 3 h timestep at local time.

GMDD
6, 3381–3426, 2013

4 Data

4.1 ERA-Interim

ERA-I is a global atmospheric reanalysis produced by the ECMWF. The ERA-Interim data assimilation system contains many improvements both in the forecasting model and analysis methodology relative to ECMWF's previous reanalysis, ERA-40, including the use of 4-dimensional variational analysis, a revised humidity analysis, the use of variational bias correction for satellite data, and other improvements in data handling (Dee et al., 2011). ERA-I provides meteorological data from 1 January 1979 and continues to be extended in near-real time. Gridded products include a large variety of 3 hourly (00:00, 03:00, 06:00, 09:00, 12:00, 15:00, 18:00, and 21:00 UTC) grid-surface fields (GRID) and 6 hourly (00:00, 06:00, 12:00, and 18:00 UTC) upper-atmosphere products available on 60 pressure levels (PL) with top of the atmosphere located at 1 mb. ERA-I relies on a 4-D-VAR system which uses observations within the windows of 15:00–03:00 UTC and 03:00–15:00 UTC (in the next day) to initialize forecast simulations starting at 00:00 UTC and 12:00 UTC, respectively. In order to allow sufficient spin-up, the first nine hours of the forecast simulations are not used. All fields used in this study where extracted on the ECMWF reduced gaussian N128 grid ($0.75^\circ \times 0.75^\circ$). Six PLs are used in this study covering the range of 1000–500 mb (1000, 925, 850, 775, 650, 500), corrosponding to approximately an elevation range of 150–5500 m a.s.l. Fields obtained have been discussed in Sect. 3.

4.2 Evaluation datasets

See Table 1 for an overview (by variable) of the evaluation (OBS) datasets used in this study. Hourly measurements from the MeteoSwiss automatic meteorological network (ANETZ) are used to evaluate T, Rh, Ws, P. This network covers 40 stations ranging 1132–3580 m a.s.l. and represents well, both high mountain locations and valleys. The SLF IMIS stations are used to evaluate T, Rh, Ws. This network is biased

GMDD
6, 3381–3426, 2013

towards high alpine locations (there are few valley stations) but represents topographical heterogeneity in terms of slope and aspect better than ANETZ stations. Network elevation range is 1562–3341 m a.s.l. Ten-minute measurements from the Alpine Surface Radiation Budget network (ASRB) are used to evaluate both SW↓ and LW↓ fluxes as well as T, Rh, Ws, (Marty et al., 2002). This network has 9 stations ranging 370–3580 m a.s.l. All OBS data sources where aggregated to daily mean values to enable comparison with ERA-I fields at a common resolution. An additional analysis on diurnal cycles required aggregation at 03:00 UTC timesteps of ERA-I. See Fig. 1 for the locations all stations used in this study and elevation distribution of stations by variable. See Sect. 2.1 for assimilation issues related to evaluation datasets.

4.3 Precipitation climatology

The CRU Alpine precipitation dataset was used as the climatology in the precipitation scheme. It provides monthly precipitation totals, for the period 1800–2003, gridded at 10 arc-minute resolution over the Alpine region. The dataset is based on 192 long-term homogenized precipitation series from meteorological stations across the study domain and a high-resolution precipitation climatology for the period 1971–1990. Full details are available in Efthymiadis et al. (2006).

4.4 Data quality control

OBS values outside acceptable limits were removed automatically by applying physically plausible thresholds to all datasets. Non-changing values beyond prescribed time limits were also screened out (e.g. indicating iced wind propeller). These checks follow the methods of Meek and Hatfield (1994). Discontinuous datasets are valid as the testing strategy follows a point by point comparison between ERA-I and observations, therefore only data that exists at a given time and location in both ERA-I and observations is carried through to the analysis. This ensures that the maximum possible quantity of valid data was used in the study and error-prone gap-filling unescessary. In

GMDD
6, 3381–3426, 2013

aggregation we were careful to ensure only complete data sets where used in summed values and acceptable levels of missingness (5 % threshold) was allowed in averaging procedures in the interest of preserving data. No missingness was tolerated in summation calculations. Further details are given in the text where relevant.

5 Experiments

5.1 Location

The study region contains the entire Swiss Alps and uses 19 ERA-I gridboxes to cover all observations that are used to evaluate the methods. Switzerland contains one of the most densely observed mountain regions in the world and, therefore, is a suitable region within which to evaluate this method and specifically its performance with respect to vertical information, as it covers a large elevation gradient of 195–4634 m a.s.l. (Fig. 1).

5.2 Setup

The experimental strategy is as follows: results of the current methods (TopoSCALE) are compared to (1) unscaled grid level ERA-I fields (GRID) and (2) reference methods (REF), where appropriate. TopoSCALE, GRID and REF are all computed on 3 h timestep and then aggregated to daily values to be assessed against the OBS datasets (Sect. 4.2). Results are presented as daily means unless otherwise stated. Statistical evaluation is primarily performed using the correlation coefficient (R), the root mean squared error (RMSE) and bias (BIAS) in order to test for systematic errors, expressed simply as:

$$\text{BIAS} = \sum(\text{sim} - \text{obs}). \quad (15)$$

GMDD
6, 3381–3426, 2013

6 Results and discussion

In this section results are presented as follows: (1) pressure-level based results (T, Rh, Ws, LW↓), (2) surface based results (SW↓ and precipitation), (3) seasonal error signatures, (4) diurnal cycles, and (5) elevation effects, both absolute and relative to grid-level.

6.1 Pressure-level based results

Figure 5 gives density scatter plots for the validation dataset (OBS) against GRID, REF and TopoSCALE results (MOD) of variables computed based on pressure level data (with exception of SW↓). A density plot is used because of the large number of points plotted (e.g. $\sim 10^6$ in the case of T).

For T, (210 stations), TopoSCALE gives a significant improvement in R, RMSE and BIAS of T with respect to observations. Applying a fixed lapse rate (REF) improves the RMSE by 0.75 °C over grid level values whereas TopoSCALE improves RMSE by 2.66 °C. The BIAS in REF (1.5) is similar to GRID (1.62), whereas TopoScale significantly improves this (−0.02). Bias in TopoSCALE is concentrated at extremes of temperature, i.e. low temperatures are too high and high temperatures are too low.

For Rh (210 stations), TopoSCALE gives a significant improvement in the correlation and modest improvement in RMSE (due to the poorly performing cluster at high humidity). There appears to be a high degree of uncertainty in saturated conditions (i.e. measurements at or close to 100 %) in all cases. TopoSCALE shows significant improvement over GRID and REF (approximately the same performance) particulary in the interval 0–60 % which is significant for processes such as sublimation which occur in dry atmospheric conditions. Both GRID and REF seem unable to represent humidities less than 30 %.

Several discontinuities were observed in the wind timeseries that are possibly related to changing patterns of data assimilation (Fig. 7). At least one of these artifacts fits to a major data introduction (European wind profilers in 2002). Therefore, the wind

GMDD
6, 3381–3426, 2013

analysis was restricted to a three year period (1996–1998) that was stable. Comparison of distributions of wind speed show a large improvement of TopoSCALE over GRID especially in the R value and BIAS. There is still a large degree of scatter especially at high wind speeds. The most significant result is an improvement in BIAS with a shift of the distribution to the 1 : 1 line, while the GRID data is not able to represent values greater than $5\,m\,s^{-1}$.

For LW↓ (9 stations) there are clear improvements over GRID with REF and TopoSCALE due to high dependence on T. To isolate this affect, we performed an additional test where the Pirazzini model used in REF was driven with TopoSCALE T and Rh to assess how well the emmissivity based part of the TopoSCALE approach performed over the parameterisations employed in REF. This gave results of $R = 0.88$ and RMSE = 27.9, suggesting that the larger part of the improvement given by the TopoSCALE approach was due to the improved description of emissivity at grid-level. Overall, TopoSCALE gives an improved result over REF both when REF is driven by lapse derived T and Rh and TopoSCALE derived T and Rh. However, TopoSCALE gives a slight increase in BIAS over REF of $1.43\,W\,m^{-2}$.

Finally, Fig. 6 gives a comparison of TopoSCALE and TopoSCALE + wind sub-model for the ANETZ station at Natschen above Andermatt. The 2-pronged error signature (i.e. both topographic wind speed reduction and enhancement) is corrected by the sub-model. The wind sub-model is difficult to test widely as topographic location data is often not precise enough for point validation, especially where locations are peaks or ridges (i.e. flat ridge can be extracted as a 45° North face even on a 25 m DEM e.g. Fisher et al., 2004). This station was chosen for its position on a large slope well represented at the DEM resolution.

6.2 Surface based results

Figure 5 gives the density scatter plot for $SW\downarrow_{grid}$ OBS (9 stations) against GRID and TopoSCALE results (MOD) for both all-sky conditions and clear-sky conditions (defined as $K_t > 0.6$). Best RMSE performance is seen in clear sky conditions due to removal

GMDD
6, 3381–3426, 2013

of a large proportion of cloud based uncertainty. However BIAS is higher in clear-sky conditions due to residual elevation effects affecting the larger direct beam component. TopoSCALE reduces this BIAS by around 3.5 $W m^{-2}$ as well as improving the RMSE score by 5 $W m^{-2}$. BIAS is also reduced under all-sky conditions by TopoSCALE but more modestly and RMSE score is roughly equal. This indicates that TopoSCALE improves the direct beam component most as corrections focus on this part of the radiation budget. In a separate analysis the Erbs partitioning scheme for direct and diffuse SW↓ was tested. As expected the partitioning scheme adds some uncertainty (i.e. R reduced from 0.88 to 0.81/0.75 respectively under all-sky conditions). Results for direct/diffuse are negatively/positively biased (–20.4/17.2 %). Full details are not given here as this topic is well covered in the literature (e.g. Erbs et al., 1982; Ruiz-Arias et al., 2010a). Despite high uncertainty introduced in decomposition models, the reaggregation of solar components after elevation/terrain correction minimizes the potential effects in the final terrain corrected estimates (Ruiz-Arias et al., 2010a).

Two quantities are important in modelling precipitation, quantity and frequency, the former representing total inputs and the second controlling distribution of those inputs over a given period of time. Figure 7 shows one of the common problems with climate models in general – that is of "constant drizzle" i.e. a low number of dry days which is compensated for by too high frequency and low intensity precipitation (Piani et al., 2009; Manders et al., 2012). The percentage dry days of OBS is much higher (and not even overlapping) that of ERA-I GRID data. This cannot be changed by the current scheme as precipitation can not be created (to be conservative), but only distributed to the subgrid according to the scheme. A conservative approach would require a temporal redistribution of precipitation as opposed to the spatial corrections we apply in this study. Figure 8 shows that both REF and TopoSCALE improve the distribution of monthly precipitation totals, especially high intensity events accounting for approximately 50 % of mass inputs (central grey line in the figure). The dominant effect is from the lapse rate as both REF and TopoSCALE distributions are reasonably similar. Figure 9 gives monthly and annual totals for all eligible stations in the OBS dataset.

GMDD
6, 3381–3426, 2013

The improvement of TopoSCALE with the inclusion of the spatial component over REF (purely lapse-rate based), is evident with improved R, RMSE and BIAS scores. Figure 9 also highlights the improved simulation of both extremes.

6.3 Diurnal cycles

The diurnal cycle in surface and boundary-layer variables is important for the global climate system (Dai and Trenberth, 2004), and particularly in simulating daily variation in the surface energy balance. Figure 10 shows the diurnal cycle of SW↓ and T, two fields chacterised by distinctive diurnal cycles, in order to investigate the performance of the scheme at subdaily timescales. Additionally these fields represent surface (SW↓) and pressure-level (T) fields. We calculated the average of all 03:00–00:00 UTC 3 h timesteps over the entire study period for months of December and June. A subset of OBS stations is presented representing an elevation range of 370 (LOC)–3580 (JFJ) m a.s.l. In general, the diurnal cycle of SW↓ appears to be well reproduced by ERA-I. However seasonal differences are apparent with more accurate simulation in June than December as indicated by the full range of values at 12:00 UTC being more comprehensively represented. Lower amplitudes of diurnal cycles in T make the analysis less clear. In December, diurnal cycles are quite strongly smoothed at low elevation whereas cycles are virtually non-existent in the OBS data at high elevation. In June there is a degree of smoothing at low elevations but cycles are generally reproduced. However, at high elevation there is a very strong smoothing. Where TopoSCALE performs less well for T (i.e. winter and high elevation) is likely related to poor representation of surface boundary layer in ERA-I data (cf. Sect. 2.3).

6.4 Seasonal error

Figure 11 gives boxplots of deviation of daily values of MOD from OBS, as defined above and grouped according to month of the year in order to investigate seasonal patterns in the error signature. No averaging is performed, all daily mean values are

GMDD
6, 3381–3426, 2013

considered. Results for T suggests that TopoSCALE is too warm in winter and too cold in summer. The median and the majority of the 25–75 % quantile lie within a 1° error margin. The boxplot for Rh shows that TopoSCALE greatly reduces the seasonal error signal over both REF and GRID. There is an almost constant small negative bias throughout the year. If a bias correction were applied the 25–75 % quantiles would lie within a 10 % (refering to the unit of Rh) error margin. Results for Ws shows the strong bias correction by TopoSCALE throughout the year with slightly poorer performance in spring. Results for LW↓ show a negligible seasonal pattern in GRID, REF and TopoSCALE. TopoSCALE has a lower magnitude of error. Both REF and TopoSCALE show slightly larger errors in April and May (but with opposing sign). Results for SW↓ show negative bias for both all-sky and clear-sky conditions. This effect is strongest in spring/summer, possibly due to higher magnitudes of values. The TopoSCALE correction is most evident under clear-sky conditions in autumn/winter.

6.5 Elevation effects

Figure 12 shows the daily mean error of GRID, REF and TopoSCALE results (MOD) with respect to OBS as a function of relative elevation of station (e.g. station elevation – grid elevation). Each box may contain multiple stations as long as they share the same elevation difference from their respective ERA-I grid cell. The plot is binned into 400 m intervals (300 m for radiation). This analysis was performed to investigate any elevation depency of the error signal as well as to look at the effect of the different methods implemented in the ERA-I model to compute variables on pressure levels above and below the model surface (cf. Sect. 2.4). The red box represents surface data (grid-level ±200 m) in order to investigate the relative performance gain/loss close to the grid-surface. This may point to suitability of TopoSCALE outside of mountain areas.

The results for T show larger error for stations below grid (RMSE = 2.46) than above (RMSE = 1.60). This result is also slightly negatively biased. This shows that the extrapolation of data below grid level produces a poorer result and only slightly better that REF. The fact that observations tend to be colder indicates that absence of sub-grid

GMDD
6, 3381–3426, 2013

effects such as inversions could be significant in driving this bias. Above grid level there are large improvements over REF and GRID. REF shows the expected result that error related to lapse rate based approaches increases with the distance over which they are applied. The Rh plot shows that TopoSCALE is increasing positively/negatively biased with distance above/below grid level as compared to REF. However the absolute magnitude of error is much lower. Ws bias in GRID error signature is corrected by TopoSCALE (albeit slightly overcompensated above grid). TopoSCALE performs better below grid level, possibly due to lower absolute Ws magnitudes leading to lower error values.

Looking only at surface data (red-box), pressure level based results (i.e. TopoSCALE) outperform surface data based results (i.e. GRID and REF) in all cases but most significantly in T and Ws. This is quite surprising as it would seem likely that the surface data should contain more of the boundary layer effect (cf. Sect. 2.3). However, this indicates that TopoSCALE could also be usefully applied in locations close to grid level without reduced quality over surface-based data.

7 Conclusions

This study has proposed a method that can efficiently provide meteorological variables to numerical models operating at point-scale in complex terrain. In addition, it provides a means to provide driving data in remote areas. The schemes focus is on variables that can be derived from pressure-level data, however, surface fields are also computed in order to provide a consistent set of driving meteorology required by a numerical LSM. Important limitations of the approach are described in Sect. 2 but can be summarised as related to (1) assimilation issues (i.e. possible reduction in performance in data-poor areas), (2) reduced performance below grid-level (although this is not universal in gridded datasets), (3) bias in gridded climate data, and (4) sub-grid phenomena that are not resolved by the input data (such as temperature inversions). Specifically, in terms of variables computed in this study, strong improvements in the radiation scheme would

GMDD
6, 3381–3426, 2013

likely result from the availability of radiative fluxes (LW↓, $SW\downarrow^{dir}$ and $SW\downarrow^{dif}$) on pressure levels or at least at some of them. The benefit of such an improved description of vertical profiles and diffuse/direct partitioning would be of great relevance as large areas globally are subject to rugged topography (cf. Gruber, 2012; Körner et al., 2011; Meybeck et al., 2001). As an outlook, partitioned SW↓ components are now archived in the current ECWMF operational model (ECWMF, personal communication, 2012), so will likely be available in future generations of reanalysis, but possibly only at the surface. Precipitation could be improved by a more rigorous sub-model such as that proposed by e.g. Smith and Barstad (2004). We attempt to account for subgrid orographic effects such as rain-shadows by implementing a description of variability through a climatology, but this is dependent on the quality of the climatology database. However, the next generation of reanalysis (e.g. ERA-20C) are likely to deliver large improvements in this respect due to higher model resolutions improving the representation of orographic precipitation. Additionally, when used with RCM (e.g. CORDEX, the first globally integrated RCM project) or weather model it is expected that precipitation based error would be reduced significantly. In sum, the core strengths of scheme we have described in this study are that it:

1. Generally gives a large improvement in scaling of variables both over grid-based values and over the reference methods tested. This improvement is most significant in pressure-level based data.
2. Provides spatially and temporally continuous meteorological fields at point-scale which are physically consistent.
3. Provides input data in complex terrain and remote areas.
4. Is efficient and therefore can be used to derive long timeseries or data over large areas.
5. Provides a means to generate down-scaled data when statistical methods are not possible i.e. in remote, data-poor areas or future time periods.

GMDD
6, 3381–3426, 2013

Appendix A

Nomenclature

T	Air Temperature
Rh	Relative Humidity
Ws	Wind Speed
Wd	Wind Direction
SW$\downarrow$	Incoming Shortwave Radiation
LW$\downarrow$	Incoming Longwave Radiation
P	Precipitation
ϵ	Emissivity
pV	Water Vapour Pressure
σ	Stefan Boltzmann Constant
V_d	Sky View Factor
K_t	Clearness Index
i	Illumination Angle
m	Optical Path Length
θ_z	Solar Zenith Angle
k	Broadband Attenuation Coefficient
ϕ_0	Azimuth Angle
A	Slope Aspect
S	Slope Angle
δ	Binary Shadow Mask
P_{clim}	Climatology Precipitation Grid
λ	Vapour Pressure Coefficient
N	Cloud Cover

GMDD
6, 3381–3426, 2013

Appendix B

Additional equations

B1 Pressure level elevation

Conversion between pressure levels and elevation is achieved using the ERA-I field geopotential (ϕ), which is defined as the potential of the Earth's gravity field. This is converted to geopotential height (ϕ_h) by normalising by standard gravity (g_0) at sea level (Eq. 16). (ϕ_h) can be defined as the approximate elevation above sea-level (m a.s.l.) of a given pressure level

$$\phi_h = \phi/9.80665. \quad \text{(B1)}$$

B2 Wind sub-model

The wind submodel after Liston and Elder (2006). All angles are in radians. Compute the slope (wslpi) in the direction of the wind using slope (slp), wind direction (wd) and aspect (asp)

$$\text{wslpi} = \text{slp}\cos(\text{wd} - \text{asp}). \quad \text{(B2)}$$

Normalise wslpi to inteval from −0.5 to +0.5 by dividing by 2× maximum wslp (wslpMax) in simulation domain

$$\text{wslp} = \text{wslpi}/(2\text{wslpMax}). \quad \text{(B3)}$$

Normalise curvature (curve) to inteval −0.5 to +0.5 by dividing by 2 × maximum curve (curveMax) in simulation domain

$$\text{curveNorm} = \text{curve}/(2\text{curveMax}). \quad \text{(B4)}$$

GMDD
6, 3381–3426, 2013

Compute the wind speed adjustments (slpw and curvew are weighting parameters which sum to 1)

$$\text{windw} = 1 + (\text{slpw}\,\text{wslp}) + (\text{curvew}\,\text{curveNorm}). \quad \text{(B5)}$$

Compute the terrain-modified wind speed (wst) from input wind speed (ws)

$$\text{wst} = \text{ws} \cdot \text{windw}. \quad \text{(B6)}$$

Compute wind direction diverting factor (Ryan, 1977)

$$\text{thetad} = -0.5(\text{wslp})\sin(2(\text{asp} - \text{wd})). \quad \text{(B7)}$$

Compute the terrain-modified wind direction

$$\text{wdt} = \text{wd} + \text{thetad}. \quad \text{(B8)}$$

B3 Compute water vapour pressure, *pV*

Constants: $\text{es}_0 = 6.11$ (reference saturation vapor pressure (es at a certain temperature, usually 0 °C) $T_0 = 273.15$ (273.15 K, Kelvin = °C +273.15) $\text{lv} = 2.5 \times 10^6$ (latent heat of vaporization of water ($2.5 \times 10^6\,\text{J kg}^{-1}$)) $\text{Rv} = 461.5$ (gas constant for water vapor ($461.5\,\text{J K kg}^{-1}$)). Variables: RH = relative humidity (%) tair = air temperature (Kelvin)

$$es_0 = es_0 \cdot \exp\left[\text{lv}/\text{Rv}\left(\frac{1}{T_0} - \frac{1}{\text{tair}}\right)\right], \quad \text{(B9)}$$

$$pV = \frac{\text{RH} \cdot \text{es}}{100}. \quad \text{(B10)}$$

GMDD
6, 3381–3426, 2013

B4 SW↓ partitioning

Compute the clearness index, K_t:

$$K_t = \frac{SW\downarrow}{SW_{TOA}}. \quad \text{(B11)}$$

Compute SW↓ diffuse fraction:

$$kd = 0.952 - 1.041e^{-\exp(2.300-4.702K_t)}. \quad \text{(B12)}$$

B5 Precipitation factor

The precipitation factor used in REF and TopoSCALE after Liston and Elder (2006) to calculate elevation adjusted P_{sub}

$$P_{sub} = P \cdot \frac{1 + pf \cdot eD}{1 - pf \cdot eD}, \quad \text{(B13)}$$

where precipitation factor, pf = 0.27 (can vary monthly) and elevation difference between GRID and SUB is given by ed.

Acknowledgements. We would like to thank R. Philipona from MeteoSwiss for providing the ASRB data, MeteoSwiss for ANETZ dataset and the SLF for IMIS dataset and Climate Research Unit for the precipitation data. We would also like to thank M. Dall'Amico P. Pogliotti for compiling the meta-data on IMIS/ANETZ stations. We would like to thank ECMWF for availability of the reanalysis data. This project was funded by SNF Project CRYOSUB and X-Sense.

GMDD
6, 3381–3426, 2013

References

Akhtar, M., Ahmad, N., and Booij, M. J.: Use of regional climate model simulations as input for hydrological models for the Hindukush-Karakorum-Himalaya region, Hydrol. Earth Syst. Sci., 13, 1075–1089, doi:10.5194/hess-13-1075-2009, 2009. 3383

Arnold, N. and Rees, G.: Effects of digital elevation model spatial resolution on distributed calculations of solar radiation loading on a High Arctic glacier, J. Glaciol., 55, 973–984, doi:10.3189/002214309790794959, 2009. 3382

Beck, C., Grieser, J., Rudolf, B., and Schneider, U.: A new monthly precipitation climatology for the global land areas for the period 1951 to 2000, Geophysical Research Abstracts, Vol. 7, 07154, 2005. 3392

Berg, A. A.: Impact of bias correction to reanalysis products on simulations of North American soil moisture and hydrological fluxes, J. Geophys. Res., 108, 4490, doi:10.1029/2002JD003334, 2003. 3385

Blandford, T. R., Humes, K. S., Harshburger, B. J., Moore, B. C., Walden, V. P., and Ye, H.: Seasonal and synoptic variations in near-surface air temperature lapse rates in a mountainous basin, J. Appl. Meteorol. Climatol., 47, 249–261, doi:10.1175/2007JAMC1565.1, 2008. 3392

Cline, D. W.: Snow surface energy exchanges and snowmelt at a continental, midlatitude Alpine site, Water Resour. Res., 33, 689–701, 1997. 3386

Dai, A. and Trenberth, K.: The diurnal cycle and its depiction in the Community Climate System Model, J. Climate, 17, 930–951, 2004. 3400

Daly, C., Neilson, R. P., and Phillips, D. L.: A statistical-topographic model for mapping climatological precipitation over mountainous terrain, J. Appl. Meteorol., 33, 140–158, 1994. 3384, 3392

Daly, C., Gibson, W. P., Taylor, G. H., Johnson, G. L., and Pasteris, P.: A knowledge-based approach to the statistical mapping of climate, Clim. Res., 22, 99–113, 2002. 3384

Dee, D. P., Uppala, S. M., Simmons, A. J., Berrisford, P., Poli, P., Kobayashi, S., Andrae, U., Balmaseda, M. A., Balsamo, G., Bauer, P., Bechtold, P., Beljaars, A. C. M., van de Berg, L., Bidlot, J., Bormann, N., Delsol, C., Dragani, R., Fuentes, M., Geer, a. J., Haimberger, L., Healy, S. B., Hersbach, H., Hólm, E. V., Isaksen, L., Kållberg, P., Köhler, M., Matricardi, M., McNally, A. P., Monge-Sanz, B. M., Morcrette, J.-J., Park, B.-K., Peubey, C., de Rosnay, P., Tavolato, C., Thépaut, J.-N., and Vitart, F.: The ERA-Interim reanalysis: configuration and

GMDD
6, 3381–3426, 2013

performance of the data assimilation system, Q. J. Roy. Meteor. Soc., 137, 553–597, doi:10.1002/qj.828, 2011. 3394
Dozier, J. and Frew, J.: Rapid calculation of terrain parameters for radiation modeling from digital elevation data, Trans. Geosci. Remote Sens., 28, 963–969, 1990. 3390
Dubayah, R. and Rich, P.: Topographic solar radiation models for GIS, Int. J. Geogr. Inf. Sci., 9, 405–419, 1995. 3390
ECMWF: IFS DOCUMENTATION – Cy37r2 PART II : DATA ASSIMILATION, ECMWF, 1–174, available at: http://www.ecmwf.int/research/ifsdocs/CY37r2/index.html, last access: 22 June 2013, 2011. 3385, 3387
Efthymiadis, D., Jones, P. D., Briffa, K. R., Auer, I., Böhm, R., Schöner, W., Frei, C., and Schmidli, J.: Construction of a 10-min-gridded precipitation data set for the Greater Alpine Region for 1800–2003, J. Geophys. Res., 111, D01105, doi:10.1029/2005JD006120, 2006. 3395
Erbs, D., Klein, S., and Duffie, J.: Estimation of the diffuse radiation fraction for hourly, daily and monthly-average global radiation, Sol. Energy, 28, 293–302, 1982. 3399
Fiddes, J. and Gruber, S.: TopoSUB: a tool for efficient large area numerical modelling in complex topography at sub-grid scales, Geosci. Model Dev., 5, 1245–1257, doi:10.5194/gmd-5-1245-2012, 2012.
Fisher, P., Wood, J., and Cheng, T.: Where is Helvellyn? Fuzziness of multi-scale landscape morphometry, T. I. Brit. Geogr., 29, 106–128, 2004. 3384, 3391
Frauenfeld, O. W.: Climate change and variability using European Centre for Medium-Range Weather Forecasts reanalysis (ERA-40) temperatures on the Tibetan Plateau, J. Geophys. Res., 110, D02101, doi:10.1029/2004JD005230, 2005. 3398
Früh, B., Schipper, J. W., Pfeiffer, A., and Wirth, V.: A pragmatic approach for downscaling precipitation in alpine-scale complex terrain, Meteorol. Z., 15, 631–646, doi:10.1127/0941-2948/2006/0137, 2006. 3383
Giorgi, F.: Regional climate modeling: status and perspectives, J. Phys. IV, 139, 101–118, doi:10.1051/jp4:2006139008, 2006. 3391
Gruber, S.: Derivation and analysis of a high-resolution estimate of global permafrost zonation, The Cryosphere, 6, 221–233, doi:10.5194/tc-6-221-2012, 2012. 3383
3403

GMDD
6, 3381–3426, 2013

Gubler, S., Fiddes, J., Keller, M., and Gruber, S.: Scale-dependent measurement and analysis of ground surface temperature variability in alpine terrain, The Cryosphere, 5, 431–443, doi:10.5194/tc-5-431-2011, 2011. 3382

Gubler, S., Gruber, S., and Purves, R. S.: Uncertainties of parameterized surface downward clear-sky shortwave and all-sky longwave radiation., Atmos. Chem. Phys., 12, 5077–5098, doi:10.5194/acp-12-5077-2012, 2012. 3388

Hagemann, S., Chen, C., Haerter, J. O., Heinke, J., Gerten, D., and Piani, C.: Impact of a statistical bias correction on the projected hydrological changes obtained from three GCMs and two hydrology models, J. Hydrometeorol., 12, 556–578, doi:10.1175/2011JHM1336.1, 2011. 3385

Helgason, W. and Pomeroy, J. W.: Characteristics of the near-surface boundary layer within a mountain valley during winter, J. Appl. Meteorol. Climatol., 51, 583–597, doi:10.1175/JAMC-D-11-058.1, 2012. 3386

Huffman, G. J., Bolvin, D. T., Nelkin, E. J., Wolff, D. B., Adler, R. F., Gu, G., Hong, Y., Bowman, K. P., and Stocker, E. F.: The TRMM Multisatellite Precipitation Analysis (TMPA): quasi-global, multiyear, combined-sensor precipitation estimates at fine scales, J. Hydrometeorol., 8, 38–55, doi:10.1175/JHM560.1, 2007. 3392

Jarosch, A. H., Anslow, F. S., and Clarke, G. K. C.: High-resolution precipitation and temperature downscaling for glacier models, Clim. Dynam., 38, 391–409, doi:10.1007/s00382-010-0949-1, 2012. 3383, 3387

Konzelmann, T., van de Wal, R. S., Greuell, W., Bintanja, R., Henneken, E. A., and Abe-Ouchi, A.: Parameterization of global and longwave incoming radiation for the Greenland Ice Sheet, Global Planet. Change, 9, 143–164, 1994. 3388, 3392

Körner, C., Paulsen, J., and Spehn, E. M.: A definition of mountains and their bioclimatic belts for global comparisons of biodiversity data, Alp. Bot., 121, 73–78, doi:10.1007/s00035-011-0094-4, 2011. 3403

Kotlarski, S. and Block, A.: Regional climate model simulations as input for hydrological applications : evaluation of uncertainties, Adv. Geosci.,5, 119–125, 2005. 3383

Kotlarski, S., Paul, F., and Jacob, D.: Forcing a Distributed Glacier Mass Balance Model with the Regional Climate Model REMO, Part I: Climate Model Evaluation, J. Climate, 23, 1589–1606, 2010. 3384

Kunkel, K.: Simple procedures for extrapolation of humidity variables in the mountainous western United States, J. Climate, 2, 656–669, 1989. 3392

GMDD
6, 3381–3426, 2013

Liston, G. E. and Elder, K.: A meteorological distribution system for high-resolution terrestrial modeling (MicroMet), J. Hydrometeorol., 7, 217–234, 2006. 3382, 3383, 3391, 3392, 3393, 3405, 3407

Liston, G. E. and Sturm, M.: A snow-transport model for complex terrain, J. Glaciol., 44, 498–516, 1998. 3388

Machguth, H., Paul, F., Kotlarski, S., and Hoelzle, M.: Calculating distributed glacier mass balance for the Swiss Alps from regional climate model output: a methodical description and interpretation of the results, J. Geophys. Res, 114, 1930–1990, 2009. 3384

Manders, A. M. M., van Meijgaard, E., Mues, A. C., Kranenburg, R., van Ulft, L. H., and Schaap, M.: The impact of differences in large-scale circulation output from climate models on the regional modeling of ozone and PM, Atmos. Chem. Phys., 12, 9441–9458, doi:10.5194/acp-12-9441-2012, 2012. 3399

Maraun, D. and Wetterhall, F.: Precipitation downscaling under climate change: recent developments to bridge the gap between dynamical models and the end user, Rev. Geophys., 48, 1–38, 2010. 3383

Marks, D., Domingo, J., Susong, D., Link, T., and Garen, D.: A spatially distributed energy balance snowmelt model for application in mountain basins, Hydrol. Process., 13, 1935–1959, 1999. 3383

Marty, Ch., Philipona, R., Fröhlich, C., and Ohmura, A.: Altitude dependence of surface radiation fluxes and cloud forcing in the alps: results from the alpine surface radiation budget network, Theor. Appl. Climatol., 72, 137–155, 2002. 3395

Meek, D. and Hatfield, J.: Data quality checking for single station meteorological databases, Agr. Forest Meteorol., 69, 85–109, 1994. 3395

Mesinger, F., DiMego, G., Kalnay, E., Mitchell, K., Shafran, P. C., Ebisuzaki, W., Jović, D., Woollen, J., Rogers, E., Berbery, E. H., Ek, M. B., Fan, Y., Grumbine, R., Higgins, W., Li, H., Lin, Y., Manikin, G., Parrish, D., and Shi, W.: North American Regional Reanalysis, B. Am. Meteorol. Soc., 87, 343–360, doi:10.1175/BAMS-87-3-343, 2006. 3387

Meybeck, M., Green, P., and Vörösmarty, C.: A New Typology for Mountains and Other Relief Classes, Mt. Res. Dev., 21, 34–45, 2001. 3403

New, M., Lister, D., Hulme, M., and Makin, I.: A high-resolution data set of surface climate over global land areas, Clim. Res., 21, 1–25, 2002. 3392

Oliphant, E.: Spatial variability of surface radiation fluxes in mountainous terrain, J. Appl. Meteorol., 42, 113–128, 2003. 3393

GMDD

6, 3381–3426, 2013

Pereira-Cardenal, S. J., Riegels, N. D., Berry, P. A. M., Smith, R. G., Yakovlev, A., Siegfried, T. U., and Bauer-Gottwein, P.: Real-time remote sensing driven river basin modeling using radar altimetry, Hydrol. Earth Syst. Sci., 15, 241–254, doi:10.5194/hess-15-241-2011, 2011. 3383

Perez, R., Ineichen, P., Seals, R., and Zelenka, A.: Making full use of the clearness index for parameterizing hourly insolation conditions, Sol. Energy, 45, 111–114, 1990. 3390

Piani, C., Haerter, J. O., and Coppola, E.: Statistical bias correction for daily precipitation in regional climate models over Europe, Theor. Appl. Climatol., 99, 187–192, doi:10.1007/s00704-009-0134-9, 2009. 3399

Pirazzini, R., Nardino, M., Orsini, A., Calzolari, F., Georgiadis, T., and Levizzani, V.: Parameterization of the downward longwave radiation from clear and cloudy skies at Ny Alesund (Svalbard), International Radiation Symposium (IRS), 24–29 July, St. Petersburg, Russia, 559–562, 2000. 3392

Plüss, C.: The energy balance over an alpine snowcover: point measurements and areal distribution, Ph.D. thesis, Geograpisches Institut ETH, Zurich, 1997. 3393

Riseborough, D., Shiklomanov, N., Etzelmüller, B., Gruber, S., and Marchenko, S.: Recent advances in permafrost modelling, Permafrost Perigl. Proc., 156, 137–156, doi:10.1002/ppp.615, 2008. 3382

Ruiz-Arias, J., Alsamamra, H., Tovar-Pescador, J., and Pozo-Vázquez, D.: Proposal of a regressive model for the hourly diffuse solar radiation under all sky conditions, Energ. Convers. Manage., 51, 881–893, doi:10.1016/j.enconman.2009.11.024, 2010a. 3399

Ruiz-Arias, J. A., Cebecauer, T., Tovar-Pescador, J., and Šúri, M.: Spatial disaggregation of satellite-derived irradiance using a high-resolution digital elevation model, Sol. Energy, 84, 1644–1657, doi:10.1016/j.solener.2010.06.002, 2010b. 3389

Ryan, B.: A mathematical model for diagnosis and prediction of surface winds in mountainous terrain, J. Appl. Meteorol., 16, 571–584, 1977. 3406

Schmidli, J., Goodess, C. M., Frei, C., Haylock, M. R., Hundecha, Y., Ribalaygua, J., and Schmith, T.: Statistical and dynamical downscaling of precipitation: an evaluation and comparison of scenarios for the European Alps, J. Geophys. Res., 112, 1–20, doi:10.1029/2005JD007026, 2007. 3383

Schroeder, T. A., Hember, R., Coops, N. C., and Liang, S.: Validation of Solar Radiation Surfaces from MODIS and Reanalysis Data over Topographically Complex Terrain, J. Appl. Meteorol. Climatol., 48, 2441–2458, doi:10.1175/2009JAMC2152.1, 2009. 3393

GMDD
6, 3381–3426, 2013

Smith, R. and Barstad, I.: A linear theory of orographic precipitation, J. Atmos. Sci., 61, 1377–1391, 2004. 3403

Tarboton, D. G. and Luce, C. H.: Utah energy balance snow accumulation and melt model (UEB), Citeseer, Logan, Utah, 1996. 3383

Thornton, P. E., Running, S. W., and White, M. A.: Generating surfaces of daily meteorological variables over large regions of complex terrain, J. Hydrol., 190, 214–251, 1997. 3382

Vu, M. T., Raghavan, S. V., and Liong, S. Y.: SWAT use of gridded observations for simulating runoff – a Vietnam river basin study, Hydrol. Earth Syst. Sci., 16, 2801–2811, doi:10.5194/hess-16-2801-2012, 2012. 3383

Wilby, R. and Wigley, T.: Downscaling general circulation model output: a review of methods and limitations, Prog. Phys. Geogr., 21, 530–548, doi:10.1177/030913339702100403, 1997. 3383

GMDD

6, 3381–3426, 2013

Table 1. Meterological variables computed, time step they are obtained on from ERA-I and sources of validation data (assimilated/non-assimilated) and total stations used in evaluation. Differing station numbers between parameters using the same sources (e.g. T and Ws) is due to quality checks rejecting certain stations from the analysis.

Variable	Symbol	Unit	ERA-I step (hr)	Assimilated sources	Non-assimilated sources	Total stations
Air temperature	T	°C	6	ANETZ (partial)	IMIS/ASRB	210
Relative humidity	Rh	%	6	ANETZ (partial)	IMIS/ASRB	210
Wind speed	Ws	ms^{-1}	6	–	ANETZ/IMIS/ASRB	199
Precipitation	P	mmh^{-1}	3	–	ANETZ/GAUGE	500
Shortwave radiation downwards	SW↓	Wm^{-2}	3	–	ANETZ/ASRB	27
Longwave radiation downwards	LW↓	Wm^{-2}	3	–	ASRB	9

GMDD
6, 3381–3426, 2013

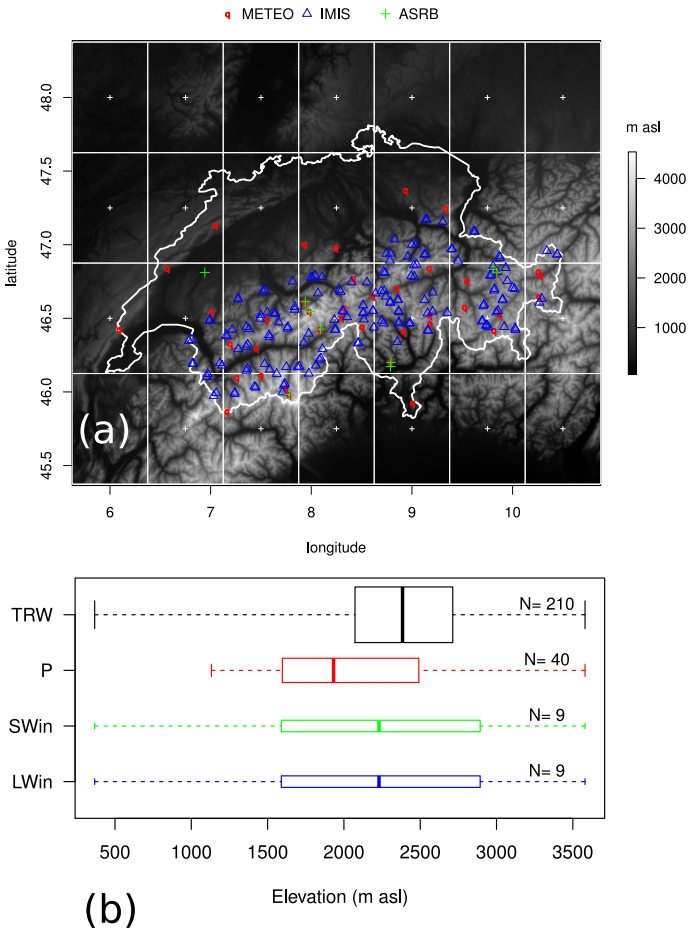

Fig. 1. (a) Experiment location and datasets with ERA-I grid used in this study. **(b)** Elevation distributions of stations by variable: *T*, Rh, Ws (TRW, 210), *P* (40), SW↓ (9), LW↓ (9). The boxes are drawn with widths proportional to the square-root of the number of stations in the group.

GMDD
6, 3381–3426, 2013

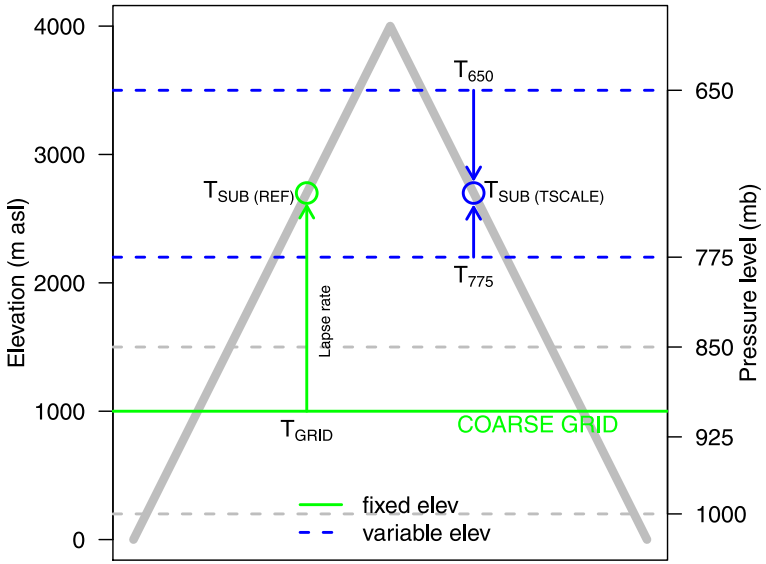

Fig. 2. Schematic of the main TopoSCALE method and experiment set up. Green line represents the coarse-grid climate data, and its position in terms of elevation and pressure levels is indicated with respect to topography (grey). Methods for describing a SUB simulation point used in this study: **(a)** grid level data (T_{GRID}), **(b)** extrapolated grid data by reference methods ($T_{SUB(REF)}$) and **(c)** TopoSCALE interpolated pressure level data ($T_{SUB(TSCALE)}$).

GMDD
6, 3381–3426, 2013

TopoSCALE: deriving surface fluxes from gridded climate data

J. Fiddes and S. Gruber

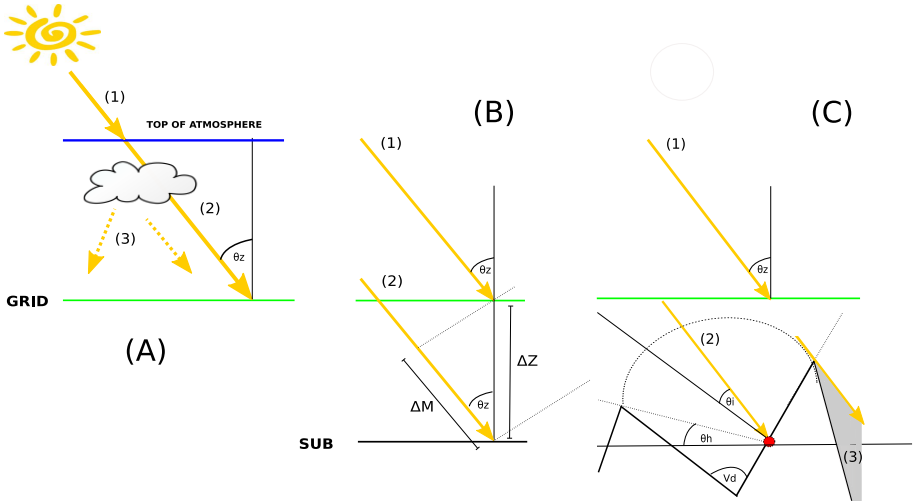

Fig. 3. Solar radiation scheme. **(A)** SW↓ at GRID is partitioned into direct (1) and diffuse (3) components through a clearness index by ratioing against extraterrestial radiation (1). **(B)** An elevation correction is applied to $SW\downarrow^{dir}_{grid}$ (1) to obtain $SW\downarrow^{dir}_{sub}$ (2) based on Δ_z,Δ_M and θ_z. **(C)** Topographic correction is applied accounting for illumination angle, θ_i, horizon angle, θ_h and sky view factor V_d.

GMDD
6, 3381–3426, 2013

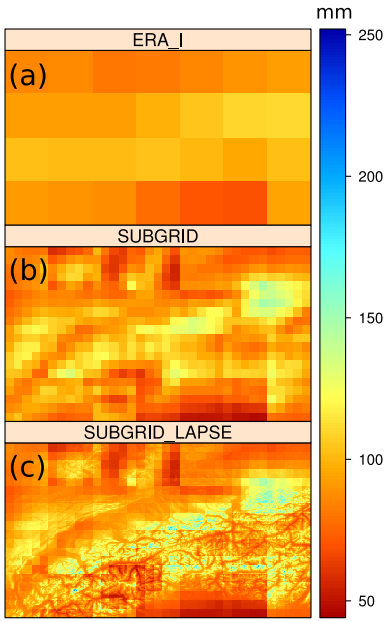

Fig. 4. Precipitation scheme steps: **(a)** ERA-I GRID precipitation, **(b)** climatology based subgrid spatial variability, **(c)** lapse-rate based vertical variability.

GMDD
6, 3381–3426, 2013

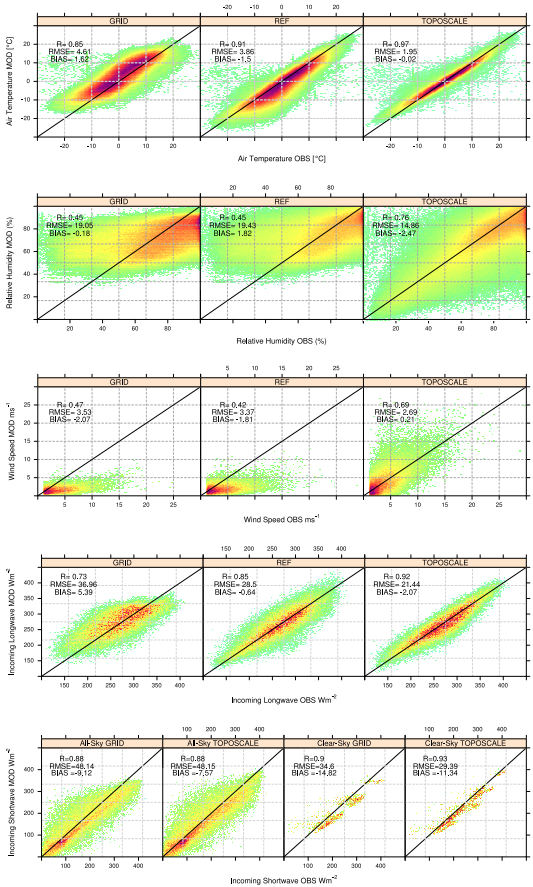

Fig. 5. Observed mean daily versus modelled *T*, Rh, Ws and LWin for GRID, REF, and TopoSCALE methods. The representation is a smoothed density plot to allow visualisation of large number plot points (IMIS-Data© 2013, SLF).

GMDD
6, 3381–3426, 2013

TopoSCALE: deriving surface fluxes from gridded climate data

J. Fiddes and S. Gruber

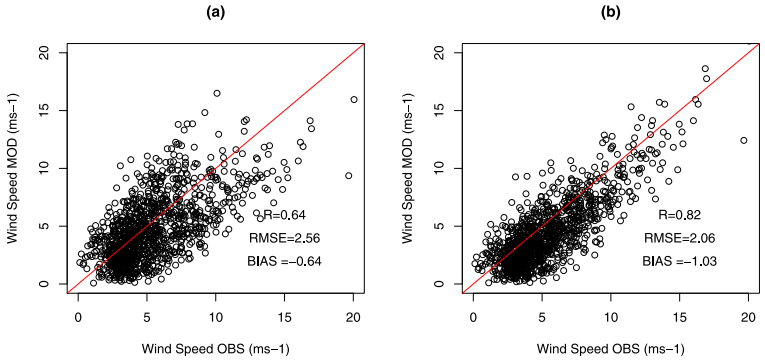

Fig. 6. Comparison of **(a)** TopoSCALE and **(b)** TopoSCALE + wind sub-model for ANETZ station at Natschen above Andermatt. The 2-pronged error signature is corrected by the sub-model. This station was chosen for its position on a large slope as opposed peak or ridge where slope angles are difficult to extract accurately from a DEM.

GMDD
6, 3381–3426, 2013

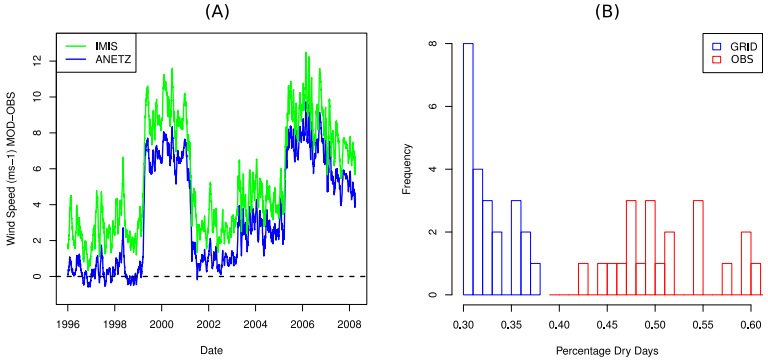

Fig. 7. Two problems encountered in the analysis. **(a)** Several discontinuities were observed in the wind time series i.e period 1999–2001 and 2005–2009. Therefore, the wind analysis was restricted to a three year period (1996–1998) that was stable. **(b)** A common problem with climate models is a low number of dry days which is compensated for by too high frequency and low intensity precipitation. The percentage dry days of OBS is much higher and distribution not even overlapping that of GRID data (IMIS-Data© 2013, SLF).

GMDD
6, 3381–3426, 2013

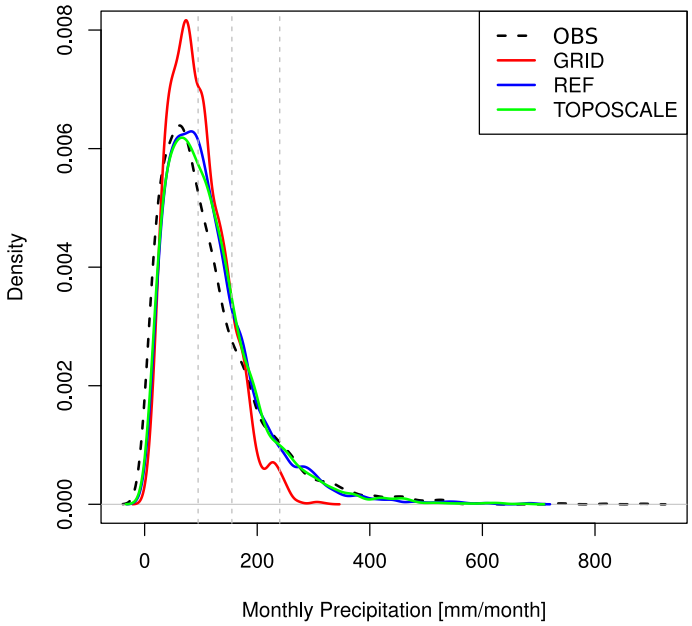

Fig. 8. PDF of GRID, REF and TopoSCALE precipitation schemes with respect to OBS. Data is monthly precipitation sums over all valid stations. Vertical lines correspond to 25–75 % quantiles of total precipitation mass (OBS). Simulation of high intensity events is improved by REF and TopoSCALE over GRID values.

GMDD
6, 3381–3426, 2013

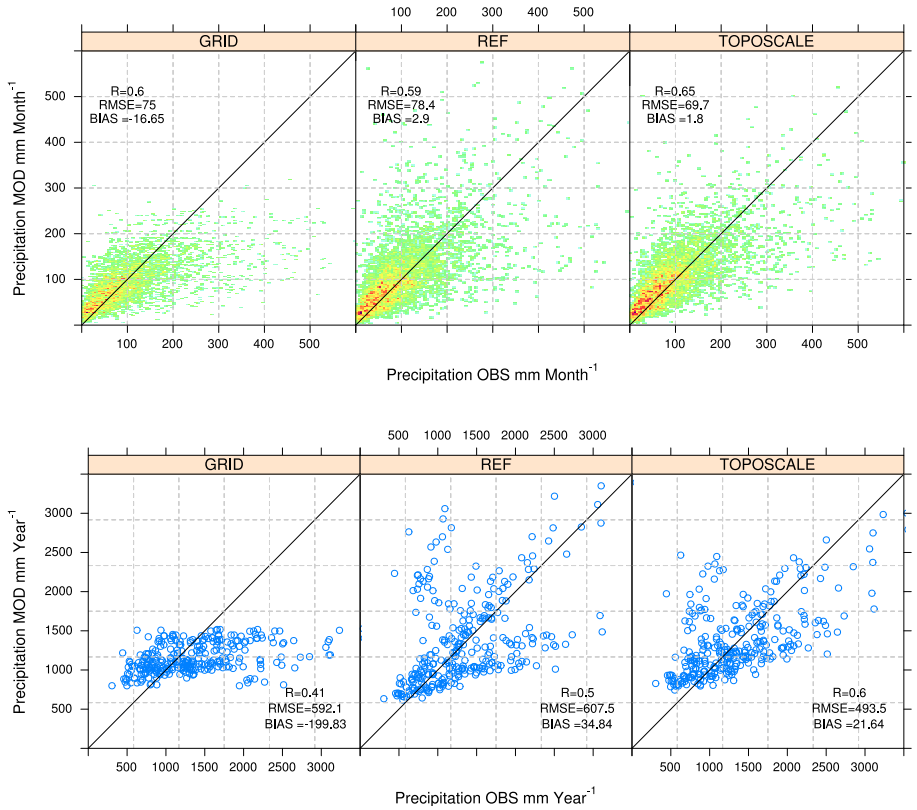

Fig. 9. Performance of TopoSCALE precipitation at monthly and annual scales compared to GRID and REF. The description of the spatial distribution of precipitation included in TopoSCALE gives improvements over a purely lapse rate based approach (REF).

GMDD
6, 3381–3426, 2013

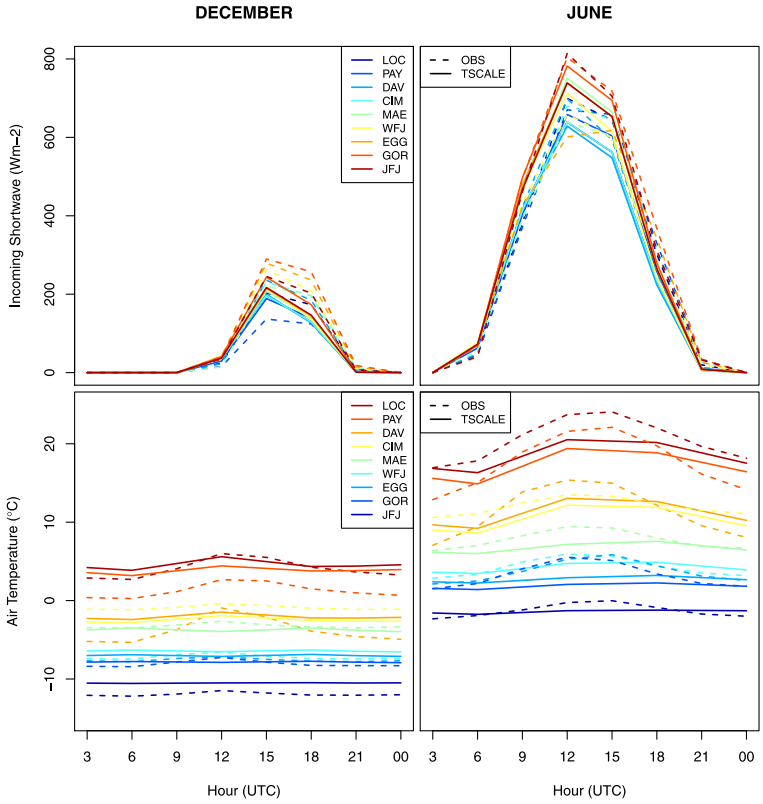

Fig. 10. The diurnal cycle of T and SW↓ as averages of all 03:00–00:00 UTC 3 h timesteps over the entire study period, for months of December and June. TopoSCALE is compared to a subset of OBS stations representing an elevation range of 370 (LOC)–3580 (JFJ) m a.s.l. TopoSCALE given by solid line, OBS given by dashed line.

GMDD
6, 3381–3426, 2013

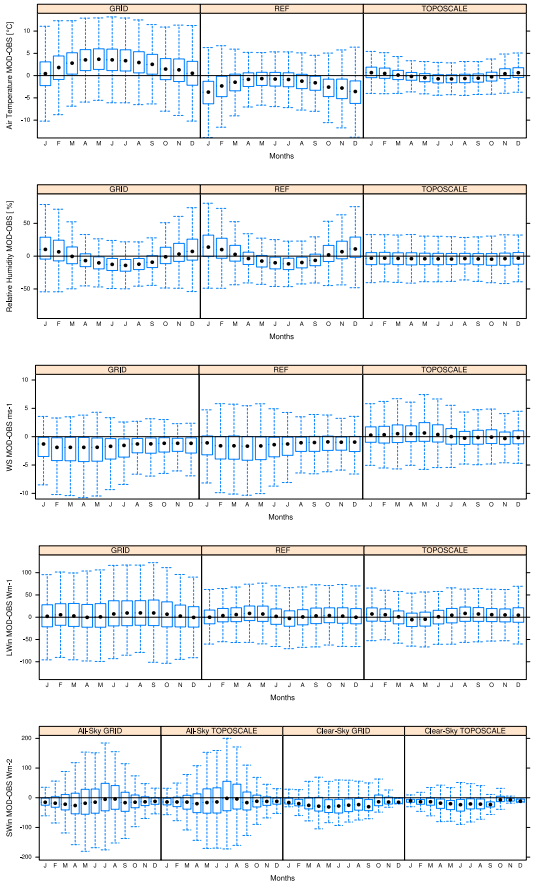

Fig. 11. Boxplot of daily air temperature error pattern over all stations as deviation from measured values, grouped by month i.e. no averaging is performed which may hide a potential seasonal signal. TopoSCALE shows generally reduced seasonal error signal over GRID and REF (IMIS-Data© 2013, SLF).

GMDD
6, 3381–3426, 2013

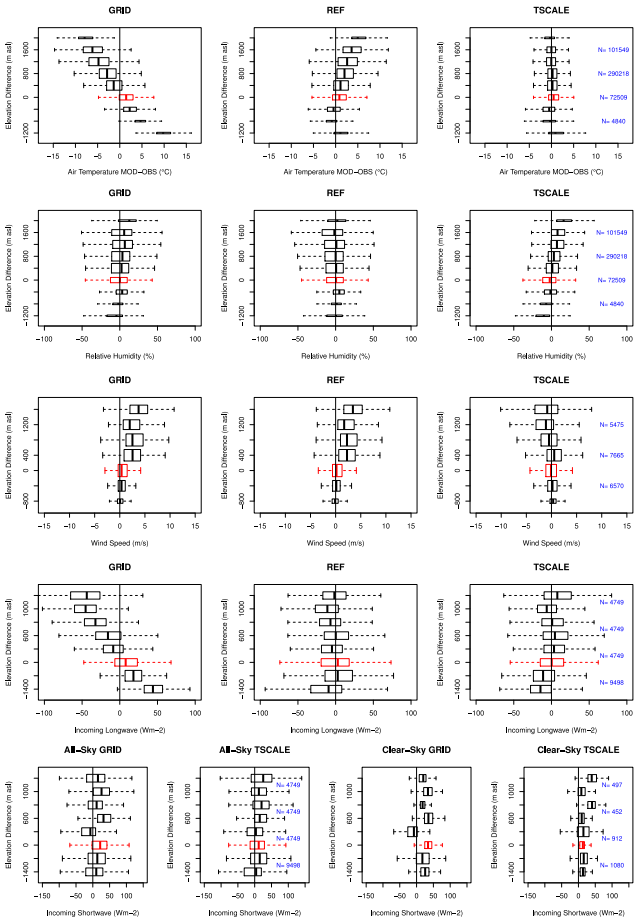

Fig. 12. Daily mean error of modelled variables with respect to observations (OBS-MOD) of GRID, REF and TopoSCALE as a function of elevation of station with respect to ERA-I grid elevation (of that station). The plot is binned into 400 m intervals. The red box represents surface data (grid-level ±200 m). Number of data points in each box are given in blue (IMIS-Data© 2013, SLF).

GMDD
6, 3381–3426, 2013

TopoSCALE: deriving surface fluxes from gridded climate data

J. Fiddes and S. Gruber